International Journal of Minerals, Metallurgy and Materials
Volume 25, Number 7, July 2018, Page 800
https://doi.org/10.1007/s12613-018-1628-1

Effects of Zn content on the microstructure and the mechanical and corrosion properties of as-cast low-alloyed Mg–Zn–Ca alloys

Hong-xiang Li, Shi-kai Qin, Ying-zhong Ma, Jian Wang, Yun-jin Liu, and Ji-shan Zhang

State Key Laboratory for Advanced Metals and Materials, University of Science and Technology Beijing, Beijing 100083, China
(Received: 5 September 2017; revised: 13 March 2018; accepted: 20 March 2018)

Abstract: The effects of Zn content on the microstructure and the mechanical and corrosion properties of as-cast low-alloyed Mg–*x*Zn–0.2Ca alloys (*x* = 0.6wt%, 2.0wt%, 2.5wt%, hereafter denoted as 0.6Zn, 2.0Zn, and 2.5Zn alloys, respectively) are investigated. The results show that the Zn content not only influences grain refinement but also induces different phase precipitation behaviors. The as-cast microstructure of the 0.6Zn alloy is composed of α-Mg, Mg_2Ca, and $Ca_2Mg_6Zn_3$ phases, whereas 2.0Zn and 2.5Zn alloys only contain α-Mg and $Ca_2Mg_6Zn_3$ phases, as revealed by X-ray diffraction (XRD) and transmission electron microscopy (TEM) analyses. Moreover, with increasing Zn content, both the ultimate tensile strength (UTS) and the elongation to fracture first increase and then decrease. Among the three investigated alloys, the largest UTS (178 MPa) and the highest elongation to fracture (6.5%) are obtained for the 2.0Zn alloy. In addition, the corrosion rate increases with increasing Zn content. This paper provides an updated investigation of the alloy composition–microstructure–property relationships of different Zn-containing Mg–Zn–Ca alloys.

Keywords: Mg–Zn–Ca alloys; as-cast microstructure; mechanical properties; corrosion properties

1. Introduction

Magnesium and magnesium alloys have been receiving increased attention as biodegradable implant materials in recent years because of their similar mechanical properties to natural bone and good biodegradability in the bio-environment [1]. Among the biodegradable magnesium alloys recently developed, Mg–Zn–Ca alloy demonstrates excellent application prospects because of its high strength (yield strength > 200 MPa, ultimate tensile strength > 250 MPa), high ductility (elongation to fracture > 20%), and good biocompatibility in the human body [2–6]. To ensure good mechanical properties of Mg–Zn–Ca alloys, high Zn contents are indispensable because of the solid-solution strengthening and precipitation strengthening effects of Zn-containing intermetallics [7–13]. However, high Zn contents adversely affect the corrosion behavior of Mg–Zn–Ca alloys because the Zn-containing intermetallics formed can function as cathodes [14–16]. Thus, maintaining a balance between mechanical properties and corrosion properties is necessary for the further development of biodegradable Mg–Zn–Ca alloys.

Recently, the design of low-alloyed Mg–Zn–Ca alloys has become a topic of interest [2,17–18]. Hofstetter *et al*. [17] developed a high-strength low-alloyed Mg–1Zn–0.3Ca extrusion alloy with fine-grained microstructure by controlling the thermomechanical processing parameters. The alloy exhibited a yield strength of 240 MPa, an elongation to fracture of 30%, and low structural and mechanical anisotropy. Zhang *et al*. [18] prepared Mg–1.0Zn–0.5Ca alloy by extrusion at different temperatures, resulting in a tensile strength of 215 MPa and an elongation of 44% because of the grain refinement and the unique extrusion texture [18]. Our literature review revealed that studies on low-alloyed Mg–Zn–Ca alloys are rare, especially for low-alloyed as-cast Mg–Zn–Ca alloys. However, exploring the as-cast microstructure can be very beneficial in understanding the precipitation sequence during age-hardening treatment for the low-alloyed Mg–Zn–Ca alloys [10]. On the other hand, the ternary intermetallic phases contained in Mg–Zn–Ca alloys, which play an important role in determining the alloys' properties, remain the subject of intense discussions and

Corresponding author: Hong-xiang Li E-mail: hxli@skl.ustb.edu.cn

disputes. Thus far, the $Ca_2Mg_6Zn_3$ [19–21], $Ca_2Mg_5Zn_{13}$ [19], $Ca_2Mg_5Zn_5$ [22–23], and IM1-4 [24–25] phases have all been proposed by experimental and CALPHAD methods. Studies on the as-cast microstructure of low-alloyed Mg–Zn–Ca alloy are also useful in judging the validity of the ternary intermetallic phases previously reported.

On the basis of these aims, we here developed a group of novel low-alloyed Mg–Zn–Ca alloys by varying their Zn content. The effects of the Zn content on the as-cast microstructure and the mechanical and corrosion properties are investigated, and a relationship between the microstructure and the properties is discussed in detail.

2. Experimental

Alloys of nominal composition Mg–*x*Zn–0.2Ca (x = 0.6, 2.0, 2.5; in wt%) were prepared from pure Mg ingots (99.99wt%), pure Zn pieces (99.99wt%), and Mg–33wt%Ca master alloys. Pure Mg ingots were first heated in a low-alloy steel crucible in an electric resistance furnace under 99% CO_2 + 1% SF_6. When the magnesium melt temperature reached 660°C, pure Zn and Mg–Ca alloys were added and the melt was stirred for 2 min. The temperature of the melt was increased to 730°C, and this temperature was maintained for 15 min; the melt temperature was then decreased to 700°C, and the melt was poured into a water-cooled copper mold, where it was cooled at an average rate of 15 K/s to obtain the as-cast ingots. No homogenization treatment was carried out.

All the specimens for microstructure characterization and X-ray diffraction (XRD) analysis were prepared using standard metallographic procedures. An OLYMPUS-BX51M optical microscope and a Supra 55 field-emission scanning electron microscope with energy dispersive X-ray (EDX) analysis capability using back-scattering electron (BSE) optical mode were used to observe the microstructure of the different Zn-containing samples. The average grain size was estimated by a line intercept technique using the scanning electron microscopy (SEM) micrographs. Preliminary phase analyses of the as-cast alloys were conducted by XRD using Rigaku DMAX-RB X-ray diffractometer equipped with a Cu K_α radiation source. Detailed studies of the distribution and types of phases were conducted by transmission electron microscopy (TEM) using a Tecnai G2 F20 (200 kV) microscope equipped with a high-angle annular-dark-field scanning transmission electron microscopy (HAADF-STEM) detector and an energy-dispersive X-ray (EDX) EDAX microanalysis system. TEM specimens were prepared by twinjet electro-polishing (Tenupol-5). All specimens were ground to approximately 100 μm and electropolished in an ACII mixture solution at −20°C under a 20-V applied potential.

Dog-bone specimens with a gauge length of 35 mm, 2-mm thickness, and 10-mm width were machined for tensile tests. The tensile tests were performed on an Instron 5569 materials testing machine at a displacement rate of 1 mm/min. Three parallel specimens were used for each group in the tensile test.

Immersion tests were conducted in Hanks' balanced salt solution without glucose (HBSS) using specimens with dimensions of 10 mm × 10 mm × 2 mm cut at 1/2 the distance from the center of the ingot. All samples were ground on emery papers to 2000 grit and were then cleaned with alcohol and dried in air. Hanks' solution was prepared with bi-distilled water and high-purity chemicals according to the procedure in Ref. [26]. The pH of the solution was adjusted to be 7.4 at (37 ± 0.5)°C through the manual addition of H_3PO_4. The immersion solution was refreshed every 24 h. After being immersed for 7 d, samples were removed from the solution and cleaned with 200 g/L CrO_3 + 10 g/L $AgNO_3$ mixed solution to remove surface corrosion products without removing any amount of metallic Mg. The specimens were rinsed with distilled water, cleaned ultrasonically in acetone, and dried in air. Afterward, the surface morphologies of the samples were observed by SEM. The corrosion rate was calculated according to the equation

$$\text{Corrosion rate} = W / (AT) \quad (1)$$

where W is the weight loss (mg), A is the exposure area (cm^2), and T is the exposure time (d).

3. Results

3.1. As-cast microstructure

Fig. 1 shows the as-cast microstructure of Mg–*x*Zn–0.2Ca (x = 0.6, 2.0, 2.5; in wt%) alloys observed by OM and SEM, respectively. Fig. 1 clearly shows a decrease of grain size from 314 μm for the 0.6Zn alloys to 133 μm for the 2.5Zn alloys, indicating an obvious grain refinement with increasing Zn content. The amount of second phases distributed in the inner of grains and along the grain boundaries also increases with increasing Zn content. The second phases distributed along the grain boundaries are mainly strip-like, whereas some granular phases are also found in the inner of grains. Moreover, the strip-like second phases are gradually connected to form a semi-continuous network structure with increasing Zn content. The width of the grain boundaries for 2.5Zn alloys is largest, and the precipitation of the second phase along the grain boundaries is also more obvious.

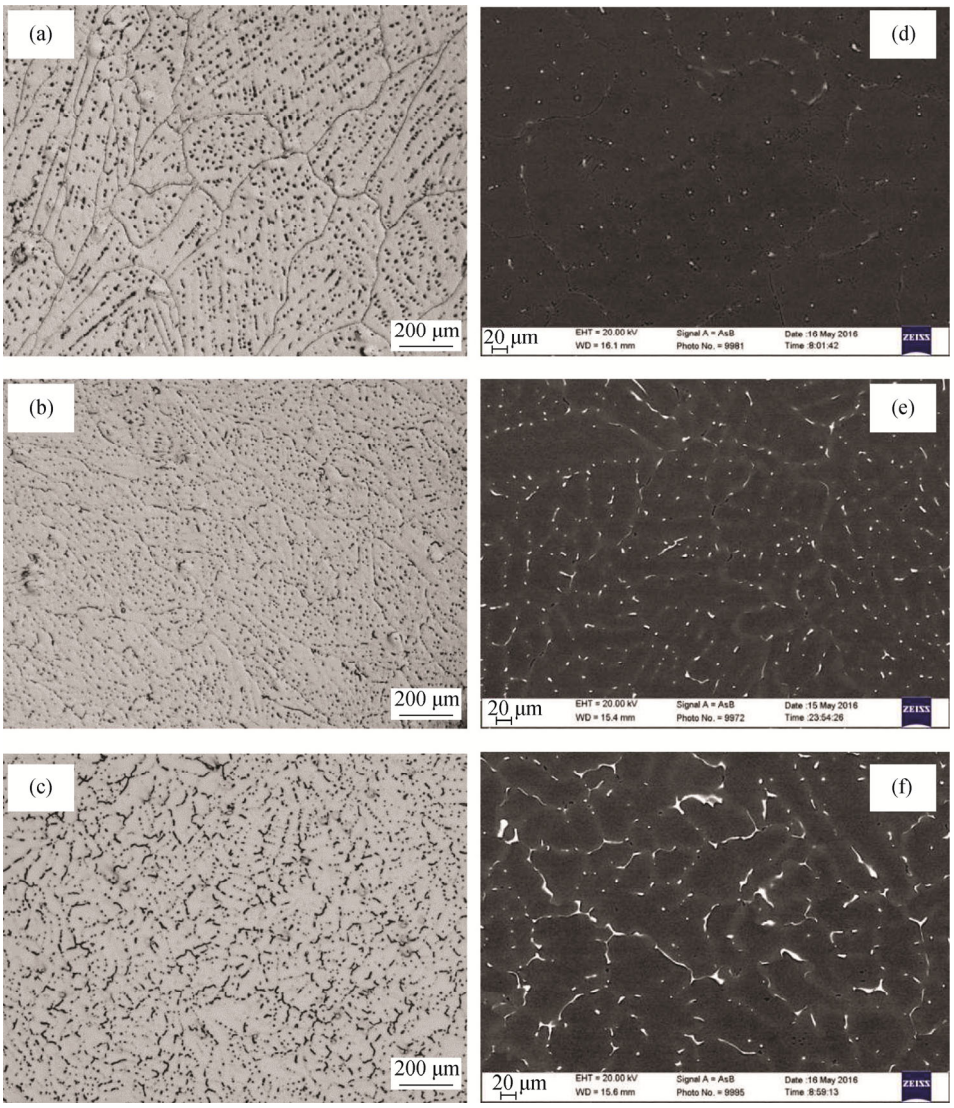

Fig. 1. The as-cast microstructure of Mg–*x*Zn–0.2Ca (*x* = 0.6, 2.0, 2.5) alloys observed by OM and SEM: (a) and (d) 0.6Zn; (b) and (e) 2.0Zn; (c) and (f) 2.5Zn.

Fig. 2 represents the XRD patterns of as-cast samples with different Zn contents. According to the phase diagrams of binary Mg–Ca and ternary Mg–Zn–Ca alloys [27], the maximum solubility of Ca and Zn in Mg is only 0.2wt% and 1.6wt%, respectively, at room temperature in the equilibrium state. Thus, with the addition of Ca and Zn above its solubility limit, excess Ca and Zn can precipitate in the form of an intermetallic as a second phase. As evident in Fig. 2, in addition to the peaks corresponding to the α-Mg matrix, peaks corresponding to $Ca_2Mg_6Zn_3$ and Mg_2Ca phases are clearly identified in the XRD pattern of the as-cast 0.6Zn alloys. However, with increasing Zn additions, such as 2.0Zn and 2.5Zn alloys, the Mg_2Ca phase is not found and only α-Mg solid solution + $Ca_2Mg_6Zn_3$ phases are observed, indicating different precipitation behaviors of high-Zn-containing alloys.

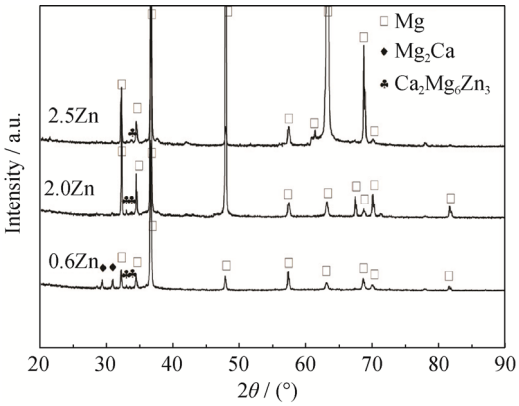

Fig. 2. The XRD patterns of as-cast Mg–*x*Zn–0.2Ca (*x* = 0.6, 2.0, 2.5) samples.

To identify the phases precipitated, TEM analyses of the 0.6Zn, 2.0Zn, and 2.5Zn alloys were performed. Fig. 3 shows TEM bright-field images of the as-cast 0.6Zn alloys and the corresponding selected-area diffraction patterns (SADPs). The alloy matrix is an α-Mg solid solution (Fig. 3(a)), as indicated by SADP images taken along the [1 $\bar{2}$ 10] zone axis shown in Fig. 3(d). Meanwhile, from the SADP analysis, $Ca_2Mg_6Zn_3$ phases with strip-like and granular morphologies (zone axis [1 $\bar{2}$ 10] and zone axis [0 0 0 1]), as shown in Figs. 3(a), 3(e) and Figs. 3(b), 3(g), are observed in the 0.6Zn alloys. The EDS analysis (Fig. 4) shows that the $Ca_2Mg_6Zn_3$ phases with strip-like and granular morphologies contain 57.79at% Mg, 24.69at% Zn, 17.52at% Ca and 66.15at% Mg, 20.27at% Zn, 13.57at% Ca, respectively. Zhang *et al*. [24–25] reported that the composition range of IM1 encompasses the compositions of both $Ca_2Mg_5Zn_5$ and $Ca_2Mg_6Zn_3$. Recently, Cao *et al*. [23] proposed that the IM1 phase is $Ca_2Mg_5Zn_5$ rather than $Ca_2Mg_6Zn_3$. From the aforementioned EDS analysis results, the composition of the current strip-like and granular phases appears to be very similar to $Ca_2Mg_6Zn_3$. The crystal structure of the phases shown in Figs. 3(e) and 3(g) also confirms that the SADP analysis is consistent with the trigonal unit cell (a = 0.97 nm, c = 1.0 nm, α = 90°, β = 90°, γ = 120°) reported for the $Ca_2Mg_6Zn_3$ structure [21]. Therefore, the phases with strip-like and granular morphologies are verified to be $Ca_2Mg_6Zn_3$. In addition to the ternary $Ca_2Mg_6Zn_3$ phases, the Mg_2Ca phase (zone axis [100]) has been recognized in the 0.6Zn alloys, which is found to coexist with $Ca_2Mg_6Zn_3$ in the form of eutectic phases, as shown in Figs. 3(c) and 3(f).

Fig. 5 shows TEM bright-field images and the corresponding SADP analysis of as-cast 2Zn alloys. From Fig. 5, 2Zn alloys are mainly composed of α-Mg solid solution and the second ternary $Ca_2Mg_6Zn_3$ phases, without the existence of Mg_2Ca. Similar to 0.6Zn alloys, $Ca_2Mg_6Zn_3$ phases also exhibit two different morphologies, i.e., strip-like and granular, as shown in Figs. 5(a) and 5(b). The SADP analysis results for the strip-like-shaped $Ca_2Mg_6Zn_3$ phase are presented in Fig. 5(d), and those for the granular-shaped $Ca_2Mg_6Zn_3$ phase are not shown here because of the similarity with Figs. 3(b) and 3(f). In addition to the two morphologies as primary phases, $Ca_2Mg_6Zn_3$ phases are also found to coexist with α-Mg in the form of eutectics (Figs. 5(c) and 5(e)). α-Mg in the eutectics is identified from SADP analysis, as shown in Fig. 5(f) (zone axis [1 $\bar{2}$ 10]).

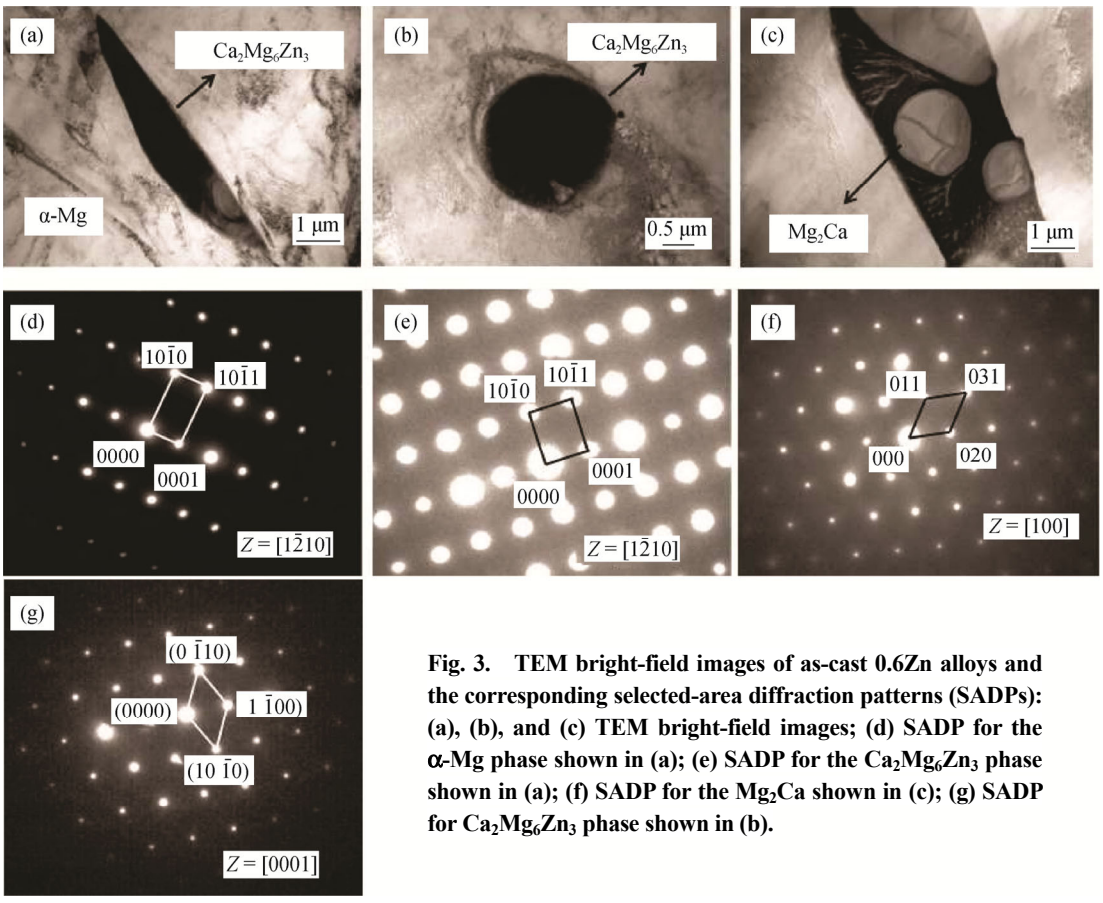

Fig. 3. TEM bright-field images of as-cast 0.6Zn alloys and the corresponding selected-area diffraction patterns (SADPs): (a), (b), and (c) TEM bright-field images; (d) SADP for the α-Mg phase shown in (a); (e) SADP for the $Ca_2Mg_6Zn_3$ phase shown in (a); (f) SADP for the Mg_2Ca shown in (c); (g) SADP for $Ca_2Mg_6Zn_3$ phase shown in (b).

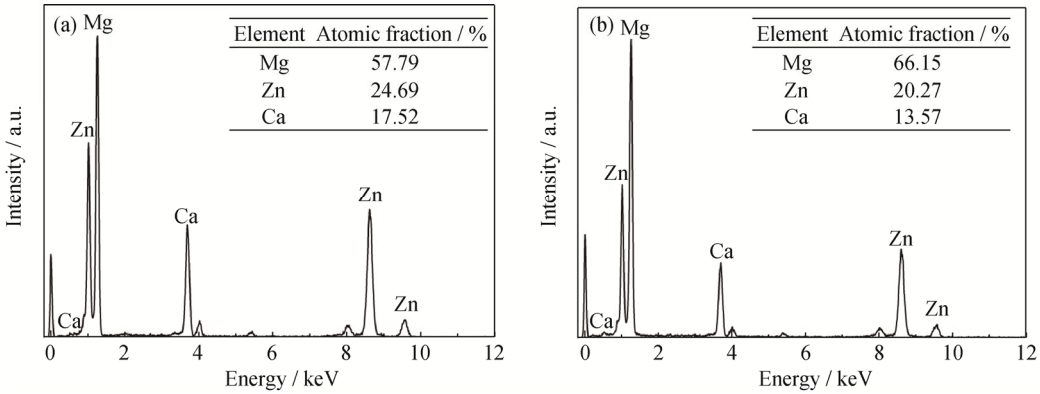

Fig. 4. EDS results for the phases with strip-like and granular morphologies shown in Figs. 3(a) and 3(b).

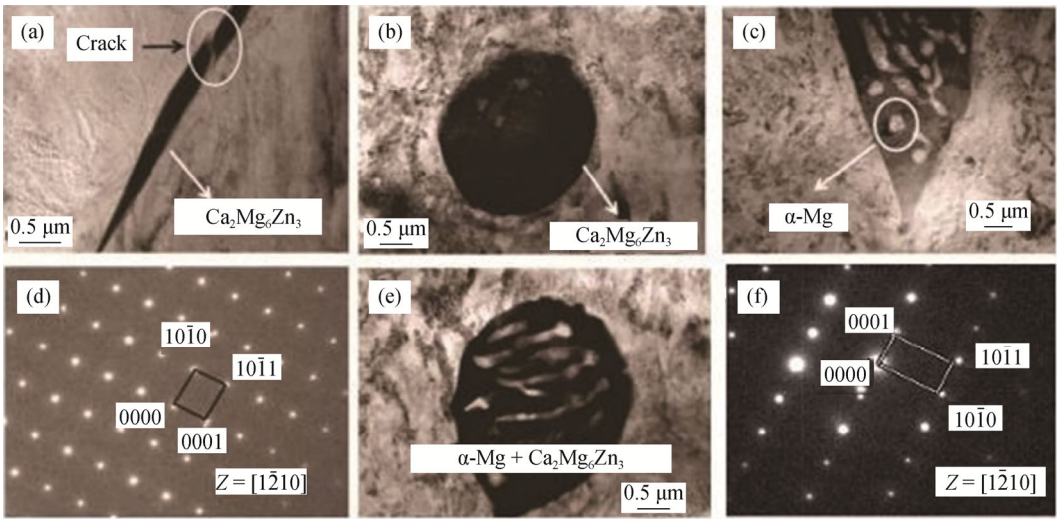

Fig. 5. TEM bright-field images of as-cast 2.0Zn alloys and their corresponding selected-area diffraction patterns (SADPs): (a), (b), (c), and (e) TEM bright-field images; (d) SADP for the $Ca_2Mg_6Zn_3$ phase shown in (a); (f) SADP for the α-Mg phase shown in (c).

Fig. 6 shows TEM bright-field images of the Mg–2.5Zn–0.2Ca alloys. Compared with Fig. 3 and Fig. 5, similar α-Mg solid solution matrix and the ternary $Ca_2Mg_6Zn_3$ phases with the strip-like and granular morphologies are also found for 2.5Zn alloys. Similar to the 2.0Zn alloys, no Mg_2Ca phase was found from the TEM analysis, which is consistent with XRD analysis results shown in Fig. 2. Combined with the TEM analysis results in Figs. 3, 5, and 6, the difference in Zn content clearly induces different phase precipitation behaviors, which will be discussed in depth in Section 4.

3.2. Mechanical and corrosion properties

Fig. 7(a) illustrates the mechanical properties of three different Zn-containing alloys; the corresponding stress–strain curve is also given as shown in Fig. 7(b). The yield strength (YS) increased slightly with increasing Zn content. The ultimate tensile strength (UTS) and the elongation at fracture first increased with increasing Zn content from 0.6wt% to 2.0wt% and then decreased when the Zn content was increased to 2.5wt%. Among the three alloys, the largest UTS (178 MPa) and the greatest elongation (6.5%) were obtained for 2.0Zn alloys.

To evaluate the corrosion properties of different Zn-containing Mg–Zn–Ca alloys, the corresponding investigations were also performed in this study. Fig. 8 shows the corrosion rate of Mg–*x*Zn–0.2Ca alloys after immersion for 168 h in a Hanks' solution at 37°C. With increasing Zn content, the corrosion rate continuously increased from 0.18 $mg \cdot cm^{-2} \cdot d^{-1}$ for the 0.6Zn alloy to 0.25 $mg \cdot cm^{-2} \cdot d^{-1}$ for the 2.5Zn alloy. For the 2.0Zn alloy, an intermediate corrosion rate of 0.21 $mg \cdot cm^{-2} \cdot d^{-1}$ was observed. Fig. 9 shows SEM micrographs of the corroded surface before and after the corrosion products were removed for three Zn-containing alloys immersed in Hanks' solution for 168 h at 37°C. Figs. 9(a), 9(c), and 9(e) shows that the insoluble corrosion layers with a number of cracks formed on the surface of alloy samples with different Zn contents. The formation of cracks

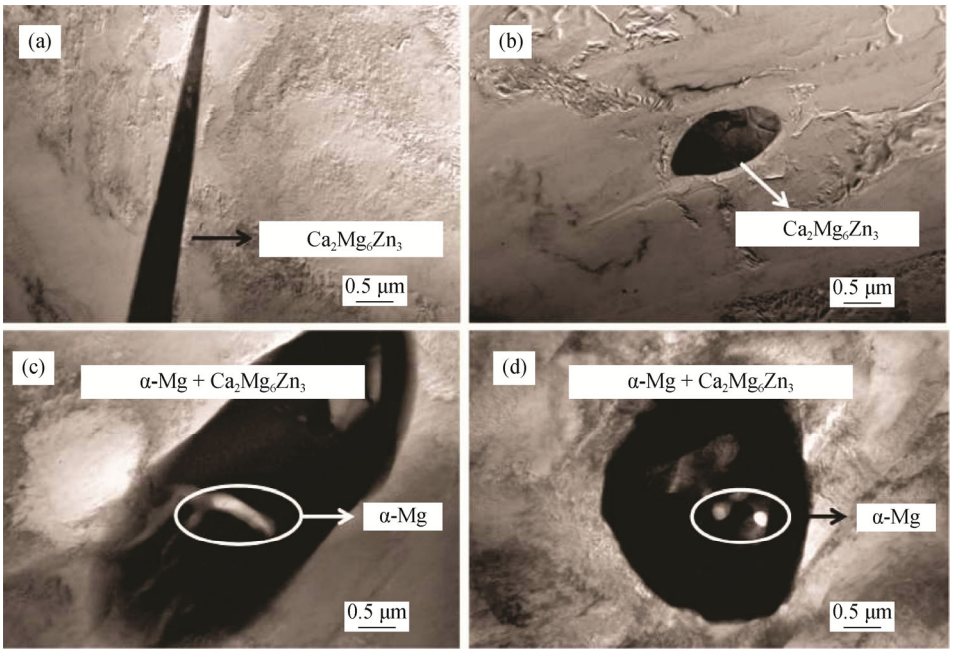

Fig. 6. TEM bright-field images of as-cast 2.5Zn alloys: (a) and (b) the bright-field images for the $Ca_2Mg_6Zn_3$ phase; (c) and (d) the bright-field images for the α-Mg and $Ca_2Mg_6Zn_3$ phase.

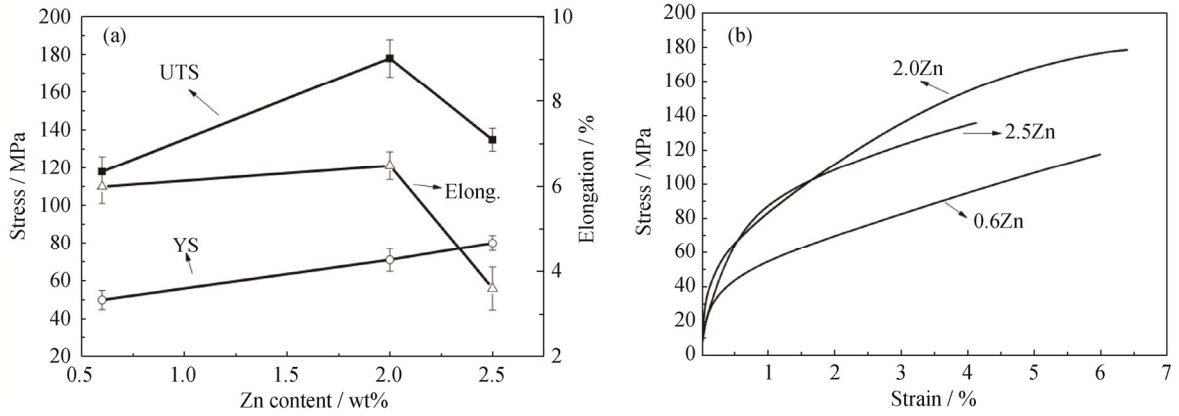

Fig. 7. The mechanical properties of three different Zn-containing alloys (a) and their corresponding stress–strain curves (b).

resulted from dehydration of the surface layer in air. With increasing Zn content, more cracks in the corrosion layer are observed, indicating more severe corrosion of this alloy. After the corrosion products were removed, different corrosion surface morphologies were observed for the alloys with different Zn contents, as shown in Figs. 9(b), 9(d), and 9(f). Numerous corrosion holes were observed for 0.6Zn alloys; the corrosion was also uneven. Compared with the corrosion of the 0.6Zn alloy samples, that of the 2.0Zn and 2.5Zn alloys was more severe. The corrosion holes were interconnected, and the corrosion cavities were formed. In particular, the ratio of corrosion holes and cavities taken up on the planar surface was larger for 2.5Zn alloys, indicating its poorest corrosion resistance.

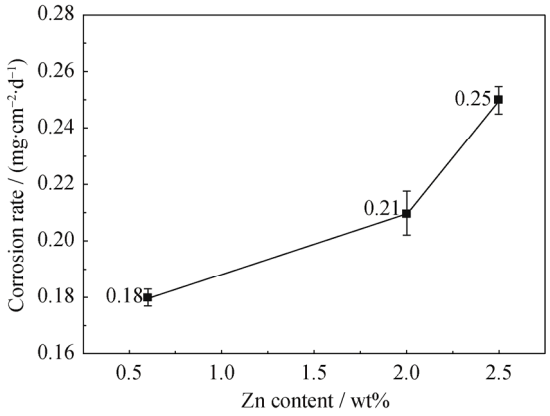

Fig. 8. The corrosion rates of Mg–*x*Zn–0.2Ca alloys (x = 0.6, 2.0, 2.5) after 168 h of immersion in a Hanks' solution at 37°C.

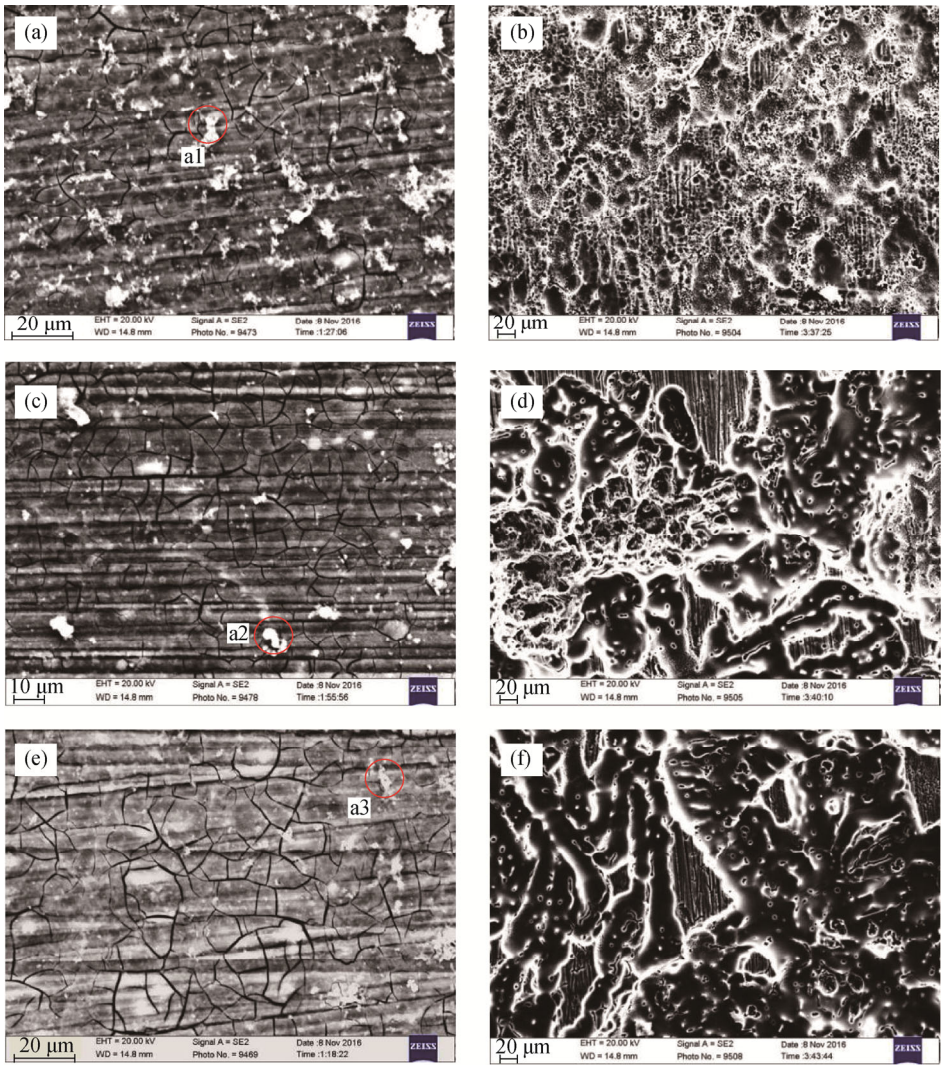

Fig. 9. SEM micrographs of the corroded surface before (a), (c), (e) and after (b), (d), (f) removal of the corrosion products for Mg–*x*Zn–0.2Ca (*x* = 0.6, 2.0, 2.5) alloys immersed in Hanks' solution for 168 h at 37°C: (a) and (b) 0.6Zn; (c) and (d) 2.0Zn; (e) and (f) 2.5Zn.

The corrosion products on the surface of different Zn-containing alloys were also analyzed by EDS. Table 1 shows the corresponding elemental analysis results for the corrosion products marked a1, a2, and a3 in Fig. 9. The corrosion products were found to be P-rich, Ca-rich, and O-rich; the concentration of oxygen, in particular, approached 60at%. Moreover, the P/Ca atomic ratio was very similar for three different Zn-containing alloys, indicating that the corrosion products on the surface of Mg–Zn–Ca alloys investigated in this study are the Ca/P-rich compounds.

Table 1. EDS analysis of the corrosion products on the surface of Mg–*x*Zn–0.2Ca (*x* = 0.6, 2.0, 2.5) alloy samples marked a1, a2, and a3 in Fig. 9. at%

Alloys	Mg	Ca	P	O	C	Others	Point in Fig. 9
0.6Zn	9.82	12.20	9.69	57.91	9.73	Bal.	a1
2.0Zn	3.23	11.97	9.43	57.03	17.71	Bal.	a2
2.5Zn	4.04	16.58	12.21	60.29	6.17	Bal.	a3

4. Discussion

In previous studies, we reported that, in as-cast Mg–Zn–Ca alloys, Zn and Ca with concentrations as high as 3wt% [7] and 9wt% [14], respectively, can refine the grain size. We also showed that the grain refinement effects can be determined by the Zn concentration and that a critical Zn content exists for attaining the minimum grain size [28]. In the present study, we found that the critical Zn content is 2.0wt% for achieving the optimal effects of grain refinement. With further addition of Zn, grain refinement is not obvious. The grain refinement is attributed to the formation of con-

stitutional undercooling in a diffusion layer in front of the solid–liquid interface. As a result of the rejection of alloying elements (Ca and Zn) at the front of grain growth, which limits the growth stage, the grain size was decreased [29].

From the microstructure analysis shown in Figs. 3–6, we found that, when the Zn content is 0.6wt%, three phases, i.e., α-Mg + Mg_2Ca + $Ca_2Mg_6Zn_3$, can be formed in the as-cast samples. The binary phase Mg_2Ca can be embraced by the ternary phase $Ca_2Mg_6Zn_3$ and thus may serve as a nucleus for the ternary phase [28]. However, when the Zn content is 2wt% or 2.5wt%, only two phases, α-Mg + $Ca_2Mg_6Zn_3$, were observed. From the OM and SEM images shown in Fig. 1, the volume fractions of the second phases increased with increasing Zn contents, leading to more interlinked phases on the grain boundaries. That is to say, with more Zn additions, $Ca_2Mg_6Zn_3$ phases distributed along the grain boundary and in the interdendritic interstices tended to increase, whereas the Mg_2Ca phase disappeared gradually. The mixing enthalpy between Zn and Ca is −22 kJ/mol, which is much larger than those of Mg–Zn (−4 kJ/mol) and Mg–Ca (−6 kJ/mol) [30]. Therefore, with the addition of Zn, Ca atoms tend to bond with Zn atoms rather than with Mg atoms. Consequently, the precipitation of ternary phase $Ca_2Mg_6Zn_3$ becomes dominant, whereas the Mg_2Ca phase gradually disappears, consistent with the precipitations of the 2.0Zn and 2.5Zn alloys. Notably, in the α-Mg + $Ca_2Mg_6Zn_3$ eutectic phase shown in Figs. 5 and 6, α-Mg is often surrounded by $Ca_2Mg_6Zn_3$, which is speculated to be related to the diffusivities of Ca and Zn. During the formation process of the eutectic phase, more Ca than Zn will be rejected from α-Mg because of the greater diffusivity of Ca in Mg [31]. Therefore, with the higher Ca concentration around the α-Mg, $Ca_2Mg_6Zn_3$ rather than Mg–Zn intermetallic compounds will be formed, consistent with the results reported by other researchers [31–32].

We confirmed that the precipitation behaviors of Mg–Zn–Ca ternary alloys are related to the Zn/Ca atomic ratio [28,33]. Other authors have reported that, when the Zn/Ca atomic ratio is greater than 1.2, only α-Mg and $Ca_2Mg_6Zn_3$ phases are observed, whereas the ternary phases α-Mg + Mg_2Ca + $Ca_2Mg_6Zn_3$ are present when the Zn/Ca atomic ratio is less than 1.2 [28,33]. In the present study, 2.0Zn and 2.5Zn alloys with Zn/Ca atomic ratios of 6.3 and 7.9, respectively, were indeed found to be composed of two phases, i.e., α-Mg + $Ca_2Mg_6Zn_3$, which is in accordance with the aforementioned conclusion. However, for the 0.6Zn alloy, three phases, α-Mg + Mg_2Ca + $Ca_2Mg_6Zn_3$, are confirmed in the present study even though its Zn/Ca atomic ratio (1.9) is much larger than 1.2. That is, the precipitation behaviors of 0.6Zn alloy are inconsistent with the aforementioned conclusion, which has also been reported in other studies [28].

In Fig. 7, the UTS and elongation to fracture of the Mg–Zn–Ca alloy first increase with increasing Zn content and then decrease upon further addition of Zn. We reported that the ternary $Ca_2Mg_6Zn_3$ is an effective strengthening phase, whereas the binary Mg_2Ca phase, i.e., a brittle phase dispersed along grain boundaries, easily produces crack sources, which can propagate and induce brittle fracture [7–8,33]. On the basis of the aforementioned microstructure analysis of 0.6Zn alloys, the coexistence of Mg_2Ca and $Ca_2Mg_6Zn_3$ phases leads to a lower YS and UTS. With increasing Zn content, such as 2.0Zn and 2.5Zn alloys, the Mg_2Ca phases all disappear, whereas more $Ca_2Mg_6Zn_3$ phases are precipitated. Moreover, with increasing Zn contents, solid-solution strengthening is enhanced. The combination of grain refinement, solid-solution strengthening, and the precipitation strengthening of the $Ca_2Mg_6Zn_3$ secondary phase easily explains the observed increases in yield strength with increasing Zn addition. For the 2.5Zn alloys, although the precipitation amount of $Ca_2Mg_6Zn_3$ phase is increased, the precipitates distribute along a semi-continuous network-shaped grain boundary with a thick grain boundary width. This kind of grain-boundary structure weakens the bonding force of the grains and easily becomes crack initiation sites, especially in the coarse precipitates located at the triangle junction of three grains. Therefore, the UTS of 2.5Zn alloys is deteriorated. However, for the 2.0Zn alloys, the integrated effects of grain refinement, solid-solution strengthening, more secondary-phase precipitation, and a lack of a thick grain-boundary structure lead to enhanced mechanical properties.

Fig. 8 clearly shows that the corrosion resistance decreases with increasing Zn content. The standard electrode potentials of the precipitated phases in Mg–Zn–Ca alloys decrease in the order $Ca_2Mg_6Zn_3$ > α-Mg > Mg_2Ca [8,33]. Thus, the Mg_2Ca phase functions as an anode and the Mg matrix as a cathode when the Mg_2Ca-containing alloy is immersed in the solution. Similarly, the $Ca_2Mg_6Zn_3$ phase serves as a cathode and the Mg matrix acts as an anode at the interface between $Ca_2Mg_6Zn_3$ and the Mg matrix when the $Ca_2Mg_6Zn_3$-containing alloy is immersed in the solution. The microstructure analysis revealed that the 0.6Zn alloys contain three phases: α-Mg + Mg_2Ca + $Ca_2Mg_6Zn_3$. We confirmed that an Mg-, Ca-, and P- containing layer (Ca–P protective film) is formed on the surface of Mg–Zn–Ca alloy when this alloy is immersed into Hanks' solution, as shown in Fig. 9. The reaction film can protect Mg alloy

from further corrosion. When the 0.6Zn alloy is immersed into Hanks' solution, the Ca^{2+} concentration in the solution can increase quickly because of the fast dissolution of the Mg_2Ca anodic phase. Thus, the formation of a Ca–P protective layer is accelerated, in turn improving the corrosion resistance of this alloy. Therefore, this alloy exhibits the minimum corrosion rate. However, with the increase of the Zn content, such as in the 2.0Zn alloy, only α-Mg and $Ca_2Mg_6Zn_3$ phases are precipitated. Thus, the $Ca_2Mg_6Zn_3$ phase serves as a cathode and the Mg matrix acts as an anode, leading to decreased corrosion resistance. For the 2.5Zn alloys, with greater precipitation of $Ca_2Mg_6Zn_3$ phases and a thicker grain-boundary width, the galvanic corrosion between the $Ca_2Mg_6Zn_3$ phase and the Mg matrix becomes stronger, leading to the largest corrosion rate of this alloy. The poor corrosion resistance of the 2.0Zn and 2.5Zn alloys is evident from their corroded surface morphologies shown in Fig. 9. With extensive corrosion of the Mg matrix around the cathode $Ca_2Mg_6Zn_3$ phase in the two alloys, the $Ca_2Mg_6Zn_3$ phases are detached and the corrosion holes are formed. More seriously, with continuing corrosion, these corrosion holes can even connect with each other and form corrosion cavities. In turn, the corrosion cavities can further accelerate the corrosion process because of contact with more corrosive liquid, leading to more severe corrosion behaviors with increasing Zn content.

5. Conclusions

(1) With increasing Zn contents, the grain size is refined, especially from 0.6Zn alloys to 2.0Zn alloys. Moreover, the amount of secondary phases precipitated also increases with increasing Zn addition.

(2) Different phase precipitation behaviors are observed for different Zn-containing alloys. The as-cast microstructure of the 0.6Zn alloy is composed of α-Mg, Mg_2Ca, and $Ca_2Mg_6Zn_3$ phases, whereas that of the 2.0Zn and 2.5Zn alloys could only contain α-Mg and $Ca_2Mg_6Zn_3$ phases, as revealed by XRD and TEM analyses.

(3) With increasing Zn contents, the ultimate tensile strength (UTS) and elongation to fracture all first increase and then decrease. Among the three investigated alloys, the 2.0Zn alloys exhibited the largest UTS (178 MPa) and the highest elongation to fracture (6.5%), which can be explained by grain refinement, solid-solution strengthening, secondary-phase strengthening, and a lack of a thick grain-boundary structure.

(4) With increasing Zn content, the corrosion rate increases correspondingly, which can be explained from the alloys' different precipitation behaviors.

(5) This paper provides an updated investigation on the alloy composition–microstructure–property relationship for different Zn-containing Mg–Zn–Ca alloys.

Acknowledgements

This research was supported by the National Natural Science Foundation of China (No. 51671017), Fundamental Research Funds for the Central Universities (No. FRF-GF-17-B3), Beijing Laboratory of Metallic Materials and Processing for Modern Transportation, the Opening Research Fund of State Key Laboratory for Advanced Metals and Materials (Nos. 2016Z-11, 2017Z-08), and State's Key Project of Research and Development Plan (No. 2016YFB0300801).

References

[1] M.P. Staiger, A.M. Pietak, J. Huadmai, and G. Dias, Magnesium and its alloys as orthopedic biomaterials: a review, *Biomaterials*, 27(2006), No. 9, p. 1728.

[2] J. Hofstetter, M. Becker, E. Martinelli, A.M. Weinberg, B. Mingler, H. Kilian, S. Pogatscher, P.J. Uggowitzer, and J.F. Löffler, High-strength low-alloy (HSLA) Mg–Zn–Ca alloys with excellent biodegradation performance, *JOM*, 66(2014), No. 4, p. 566.

[3] A.C. Hänzi, A.S. Sologubenko, P. Gunde, M. Schihammer, and P.J. Uggowitzer, Design considerations for achieving simultaneously high-strength and highly ductile magnesium alloys, *Philos. Mag. Lett.* 92(2012), No. 9, p. 417.

[4] P. Gunde, A.C. Hanzi, A.S. Sologubenko, and P.J. Uggowitzer, High-strength magnesium alloys for degradable implant applications, *Mater. Sci. Eng. A*, 528(2011), No. 3, p. 1047.

[5] B.K. Kad and P.M. Hazzledine, Monte Carlo simulations of grain growth and Zener pinning, *Mater. Sci. Eng. A*, 238(1997), No. 1, p. 70.

[6] M. Hillert, Inhibition of grain growth by second-phase particles, *Acta Metall.*, 36(1988), No. 12, p. 3177.

[7] P. Yin, N.F. Li, T. Lei, L. Liu, and C. Ouyang, Effects of Ca on microstructure, mechanical and corrosion properties and biocompatibility of Mg–Zn–Ca alloys, *J. Mater. Sci. Mater. Med.*, 24(2013), No. 6, p. 1365.

[8] L. Geng, B.P. Zhang, A.B. Li, and C.C. Dong, Microstructure and mechanical properties of Mg–4.0Zn–0.5Ca alloy, *Mater. Lett.*, 63(2009), No. 5, p. 557.

[9] Y. Sun, B.P. Zhang, Y. Wang, L. Geng, and X.H. Jiao, Preparation and characterization of a new biomedical Mg–Zn–Ca alloy, *Mater. Des.*, 34(2012), p. 58.

[10] K. Kubok, L. Litynska-dobrzynska, J. Wojewoda-budka, A. Góral, and A. Debski, Investigation of structures in as-cast alloys from the Mg–Zn–Ca system, *Arch. Metall. Mater.*, 58(2013), No. 2, p. 329.

[11] L.B. Tong, M.Y. Zheng, L.R. Cheng, S. Kamado, and H.J. Zhang, Effect of extrusion ratio on microstructure, texture and mechanical properties of indirectly extruded Mg–Zn–Ca alloy, *Mater. Sci. Eng. A*, 569(2013), p. 48.

[12] Y.Z. Du, M.Y. Zheng, C. Xu, X.G. Qiao, K. Wu, X.D. Liu, G.J. Wang, and X.Y. Lü, Microstructures and mechanical properties of as-cast and as-extruded Mg–4.50Zn–1.13Ca (wt%) alloys, *Mater. Sci. Eng. A*, 576(2013), p. 6.

[13] M. Bamberger, G. Levi, and J.B.V. Sande, Precipitation hardening in Mg–Ca–Zn alloys, *Metall. Mater. Trans. A*, 37(2006), No. 2, p. 481.

[14] H.R. Bakhsheshi-Rad, M.R. Abdul-Kadir, M.H. Idris, and S. Farahany, Relationship between the corrosion behavior and the thermal characteristics and microstructure of Mg–0.5Ca–*x*Zn alloys, *Corros. Sci.*, 64(2012), p. 184.

[15] Y.W. Song, E.H. Han, D.Y. Shan, C.D. Yim, and B.S. You, The role of second phases in the corrosion behavior of Mg–5Zn alloy, *Corros. Sci.*, 60(2012), p. 238.

[16] H.R. Bakhsheshi-Rad, M.H. Idris, M.R.A. Kadir, S. Farahany, A. Fereidouni, and M.Y. Yahya, Characterization and corrosion behavior of biodegradable Mg–Ca and Mg–Ca–Zn implant alloys, *Appl. Mech. Mater.*, 121-126(2012), p. 568.

[17] J. Hofstetter, S. Rüedi, I. Baumgartner, H. Kilian, B. Mingler, E. Povoden-Karadeniz, S. Pogatscher, P.J. Uggowitzer, and J.F. Löffler, Processing and microstructure-property relations of high-strength low-alloy (HSLA) Mg–Zn–Ca alloys, *Acta Mater.*, 98(2015), p. 423.

[18] B.P. Zhang, L. Geng, L.J. Huang, X.X. Zhang, and C.C. Dong, Enhanced mechanical properties in fine-grained Mg–1.0Zn–0.5Ca alloys prepared by extrusion at different temperatures, *Scripta Mater.*, 63(2010), No. 10, p. 1024.

[19] J.B. Clark, The solid constitution in the Mg-rich region of the Mg–Ca–Zn phase diagram, *Trans. Metall. Soc. AIME*, 221(1961), p. 644.

[20] T.V. Larionova, W.W. Park, and B.S. You, A ternary phase observed in rapidly solidified Mg–Ca–Zn alloys, *Scripta Mater.*, 45(2001), No. 1, p. 7.

[21] P.M. Jardim, G. Solórzano, and J.B. Sande, Precipitate crystal structure determination in melt spun Mg–1.5wt%Ca–6wt%Zn alloy, *Microsc. Microanal.*, 8(2002), No. 6, p. 487.

[22] Y.N. Zhang, D. Kevorkov, F. Bridier, and M. Medraj, Experimentalstudy of the Ca–Mg–Zn system using diffusion couples and key alloys, *Sci. Technol. Adv. Mater.* 12(2011), No. 2, art. No. 025003.

[23] J.D. Cao, W. Thomas, R. Schäublin, and J.F. Löffler, Equilibrium ternary intermetallic phase in the Mg–Zn–Ca system, *J. Mater. Res.*, 31(2016), No. 14, p. 2147.

[24] Y.N. Zhang, D. Kevorkov, F. Bridier, and M. Medraj, Morphological and crystallographic characterizations of the Ca–Mg–Zn intermetallics appearing in ternary diffusion couples, *Adv. Mater. Res.*, 409(2012), p. 387.

[25] Y.N. Zhang, D. Kevorkov, X.D. Liu, F. Bridier, P. Chartrand, and M. Medraj, Homogeneity range and crystal structure of the $Ca_2Mg_5Zn_{13}$ compound, *J. Alloys Compd.*, 523(2012), p. 75.

[26] H. Du, Z.J. Wei, X.W. Liu, and E. Zhang, Effects of Zn on the microstructure, mechanical property and bio-corrosion property of Mg–3Ca alloys for biomedical application, *Mater. Chem. Phys.*, 125(2011), No. 3, p. 568.

[27] C.M. Liu, X.R. Zhu, and H.T. Zhou, *Phase Diagrams of Magnesium Alloys*, Central South University Press, Changsha, 2006, p. 186.

[28] D. Zander and N.A. Zumdick, Influence of Ca and Zn on the microstructure and corrosion of biodegradable Mg–Ca–Zn alloys, *Corros. Sci.*, 93(2015), p. 222.

[29]] S.S. Li, B. Tang, and D.B. Zeng, Effects and mechanism of Ca on refinement of AZ91D alloy, *J. Alloys Compd.*, 437(2007), No. 1-2, p. 317.

[30] A. Takeuchi and A. Inoue, Classification of bulk metallic glasses by atomic size difference, heat of mixing and period of constituent elements and its application to characterization of the main alloying element, *Mater. Trans.*, 46 (2005), No. 12, p. 2817.

[31] G. Levi, S. Avraham, A. Ziberov, and M. Bamberger, Solidification, solution treatment and age hardening of a Mg–1.6 wt.% Ca–3.2 wt.% Zn alloy, *Acta Mater.*, 54(2006), No. 2, p. 523.

[32] Y. Lu, A.R. Bradshaw, Y.L. Chiu, and I.P. Jones, Effects of secondary phase and grain size on the corrosion of biodegradable Mg–Zn–Ca alloys, *Mater. Sci. Eng. C*, 48(2015), p. 480.

[33] E.L. Zhang and L. Yang, Microstructure, mechanical properties and bio-corrosion properties of Mg–Zn–Mn–Ca alloy for biomedical application, *Mater. Sci. Eng. A*, 497(2008), No. 1-2, p. 111.